ARMY RESEARCH LABORATORY

Temperature Measurements in an Ethylene-Air-Opposed Flow Diffusion Flame

by Matthew S. Kurman, John M. Densmore, Chol-Bum M. Kweon, and Kevin L. McNesby

ARL-TR-5870 **January 2012**

NOTICES

Disclaimers

The findings in this report are not to be construed as an official Department of the Army position unless so designated by other authorized documents.

Citation of manufacturer's or trade names does not constitute an official endorsement or approval of the use thereof.

Destroy this report when it is no longer needed. Do not return it to the originator.

Army Research Laboratory
Aberdeen Proving Ground, MD 21005-5066

ARL-TR-5870 **January 2012**

Temperature Measurements in an Ethylene-Air-Opposed Flow Diffusion Flame

Matthew S. Kurman
Oak Ridge Associated Universities

John M. Densmore
Lawrence Livermore National Laboratory

Chol-Bum M. Kweon
Vehicle Technology Directorate, ARL

Kevin L. McNesby
Weapons and Materials Research Directorate, ARL

REPORT DOCUMENTATION PAGE	Form Approved OMB No. 0704-0188

1. REPORT DATE *(DD-MM-YYYY)*	2. REPORT TYPE	3. DATES COVERED (From - To)
January 2012	Final	February 2011–September 2011

4. TITLE AND SUBTITLE
Temperature Measurements in an Ethylene-Air-Opposed Flow Diffusion Flame

5a. CONTRACT NUMBER

5b. GRANT NUMBER

5c. PROGRAM ELEMENT NUMBER

6. AUTHOR(S)
Matthew S. Kurman,[*] John M. Densmore,[†] Chol-Bum M. Kweon, and Kevin L. McNesby

5d. PROJECT NUMBER
1VP2J1

5e. TASK NUMBER

5f. WORK UNIT NUMBER

7. PERFORMING ORGANIZATION NAME(S) AND ADDRESS(ES)
U.S. Army Research Laboratory
ATTN: RDRL-VTP
Aberdeen Proving Ground, MD 21005-5066

8. PERFORMING ORGANIZATION REPORT NUMBER
ARL-TR-5870

9. SPONSORING/MONITORING AGENCY NAME(S) AND ADDRESS(ES)

10. SPONSOR/MONITOR'S ACRONYM(S)

11. SPONSOR/MONITOR'S REPORT NUMBER(S)

12. DISTRIBUTION/AVAILABILITY STATEMENT
Approved for public release; distribution is unlimited.

13. SUPPLEMENTARY NOTES
[*]Oak Ridge Associated Universities, 4692 Millennium Drive, Suite 101, Belcamp, MD 21017
[†]Lawrence Livermore National Laboratory, 7000 East Ave., L-227, Livermore, CA 94550

14. ABSTRACT
To support the advancement of chemical kinetic models for soot, temperature measurements were conducted on an ethylene (C_2H_4)/air-opposed flow diffusion flame at atmospheric pressure. This detailed study compares temperature measurements acquired from a single high-speed color camera optical pyrometer to thermocouple measurements and Cantera simulations for opposed flow diffusion flames. Unlike thermocouples, optical pyrometry provides a nonintrusive technique to experimentally measure flame temperature. A soot surface temperature of ~2000 K at a flame position ~2 mm above the fuel duct was acquired from the optical pyrometer. A maximum centerline flame temperature of 1898 K at 3.70 mm above the fuel duct was obtained from the thermocouple measurements. In addition, chemical kinetic modeling was conducted with Cantera and results predicted intermediate species produced during combustion and a maximum centerline flame temperature of 2077 K at 3.79 mm from the fuel duct. The results presented in this report can be used to validate and refine chemical kinetic models for soot, which ultimately can lead to advanced power-generating systems.

15. SUBJECT TERMS
optical pyrometry, thermocouple measurements, ethylene, soot, combustion

16. SECURITY CLASSIFICATION OF:			17. LIMITATION OF ABSTRACT	18. NUMBER OF PAGES	19a. NAME OF RESPONSIBLE PERSON
a. REPORT	b. ABSTRACT	c. THIS PAGE			Matthew S. Kurman
Unclassified	Unclassified	Unclassified	UU	30	19b. TELEPHONE NUMBER (*Include area code*) (410) 278-8971

Standard Form 298 (Rev. 8/98)
Prescribed by ANSI Std. Z39.18

Contents

List of Figures iv

List of Tables iv

Acknowledgments v

1. Summary 1

2. Introduction 1

3. Background 2

4. Experiment and Modeling 4

5. Results and Discussion 9

6. Conclusions 13

7. References 15

List of Symbols, Abbreviations, and Acronyms 17

Distribution List 20

List of Figures

Figure 1. Soot and NO_x regions within an equivalence ratio/temperature plane showing conventional diesel and different low-temperature combustion processes.....3

Figure 2. Schematic of the opposed flow diffusion flame burner with an enlarged view of the reaction zone. x and r are axial and radial directions, respectively. V_x and V_r are velocities in the axial and radial directions, respectively. 4

Figure 3. Camera setup for acquiring images of opposed flow diffusion flames. 5

Figure 4. Photograph of the camera setup showing various components. 6

Figure 5. Photograph of the thermocouple setup showing various components. 8

Figure 6. (a) Picture of the C_2H_4/air-opposed flow diffusion flame. (b) Reconstructed image showing the surface temperature of the C_2H_4 flame. The incorrect temperature in the blue region is caused by discrete emission. 10

Figure 7. Comparison of the Cantera simulation with the results of the pyrometry and thermocouple temperature measurements. The blue and red regions represent locations of visible light produced from the flame.....11

Figure 8. Simulation results from Cantera showing intermediate species produced during combustion, temperature profile, and local equivalence ratio. The multiplication factors are listed in parentheses. 12

Figure 9. Representation of soot and NO_x regions within an equivalence ratio/temperature plane showing Cantera simulations for different pressures. 13

List of Tables

Table 1. Initial conditions for the Cantera simulation. The mass flux of the fuel and oxidizer corresponds to the flow rates of the experiment and dimensions of the burner. 9

Acknowledgments

This research was supported in part by an appointment to the U.S. Army Research Laboratory Postdoctoral Fellowship Program administered by the Oak Ridge Associated Universities through a contract (W911QX-04-C-0129) with the U.S. Army Research Laboratory. Burner development was supported in part by the Strategic Environmental Research and Development Program of the Department of Defense. Lawrence Livermore National Laboratory is operated by Lawrence Livermore National Security, LLC, for the U.S. Department of Energy, National Nuclear Security Administration, under contract DE-AC52-07NA27344.

INTENTIONALLY LEFT BLANK.

1. Summary

Optical pyrometry and thermocouple temperature measurements were conducted on an ethylene (C_2H_4)/air-opposed flow diffusion flame at atmospheric pressure. The optical pyrometry results showed a soot surface temperature of ~2000 K at a flame position ~2 mm above the fuel duct. The pyrometry method shows an accurate temperature measurement where soot incandescence occurs. A centerline temperature profile based on thermocouple measurements (not corrected for emissivity) was reported with a maximum flame temperature of 1898 K at 3.70 mm above the fuel duct. Chemical kinetic modeling of the flame was conducted with Cantera. The results indicated that acetylene (C_2H_2), and benzene (C_6H_6), are formed in the red/orange sooting region of the flame, and methylidyne (CH) and hydroxyl (OH) are formed in the blue colored region. The modeling results predicted a maximum centerline temperature of 2077 K at 3.79 mm from the fuel duct. The experimental temperature results of this study can be used to validate and refine the chemical kinetic models, which can ultimately be used to develop and advance current power system designs.

2. Introduction

Understanding soot temperature and production can lead to the design and development of power systems that are more fuel efficient and produce less harmful emissions. In addition, the average time between failures of power systems can be increased if soot is reduced during combustion. JP-8 and Jet A, which are aviation fuels primarily used in military and commercial gas turbines, respectively, can contain aromatic hydrocarbons (Edwards and Maurice, 2001). These aromatics, which are considered as soot precursors, can form polycyclic aromatic hydrocarbons (PAHs) during combustion. Based on specification MIL-DTL-83133G (2010), up to 25% volume of JP-8 composition can be aromatic hydrocarbons. An important aspect of concealing a vehicle is reducing the plume caused by soot and incomplete combustion, which is visible during acceleration and high-load conditions. Soot not only indicates incomplete combustion and loss of efficiency, it is also a health concern. Precursors to soot, such as C_6H_6 pose many health risks (Glass et al., 2003; IARC, 1987; Rinsky et al., 1989). A focus of this study is measuring the temperature of a sooting C_2H_4/air flame.

3. Background

Soot is primarily produced from fuel-rich flames where particles can interact with one another and agglomerate to larger structures. The initial step in soot production is fuel decomposition followed by the formation of the first aromatic ring (Turns, 2000). Aliphatic fuels contain no aromatics; therefore, forming the first aromatic ring structure is the basis of soot production. Hydrocarbons that contain aromatics readily produce soot since they contain an initial supply of cyclic aromatic structures. Once the first aromatic ring is formed, other aromatic compounds can combine and grow to form larger molecular structures, PAHs, leading to the production of soot particles. A production pathway for soot can be formed by combining propargyl (C_3H_3) radicals, which are resonantly stable, to form the cyclic ring structure of C_6H_6 (Miller et al., 1992). Results also showed that self-combining C_3H_3 radicals were responsible for producing phenyl, which also contains a cyclic ring structure. Once an aromatic is formed, a repetition of two primary reactions can proceed to form soot. These reactions are shown in equations 1 and 2:

$$A_i + H \rightarrow A_i\text{-} + H_2, \quad (1)$$

and

$$A_i\text{-} + C_2H_2 \rightarrow \text{products}, \quad (2)$$

where A_i is a parent aromatic and A_i- is the radical of the aromatic hydrocarbon. Equation 1 proceeds with a hydrogen atom abstraction from the parent aromatic to form an aromatic radical and hydrogen (H_2). C_2H_2 then attaches to the aromatic radical to form polycyclic products. Equations 1 and 2 can then repeat and continue to form larger aromatic ring structures and ultimately soot (Frenklach, 2002).

To investigate soot production, it is important to understand what operating conditions, such as equivalence ratio and temperature, promote soot formation during combustion. Figure 1 is a plot from Kook et al. (2005), showing an equivalence ratio and temperature plane with modeling calculations from Kitamura et al. (2002), involving n-heptane (C_7H_{16}), combustion at a pressure of 6 MPa, and a reaction time of 2 ms. A main sooting region occurs above an equivalence ratio of ~2, whereas a region containing nitrogen oxides (NO_x) occurs at leaner equivalence ratios and higher temperatures. The behavior of a fuel element of a conventional diesel process is also shown in figure 1. An interesting observation shown in figure 1 is that there is a trade-off between soot and NO_x production. If soot is decreased by lowering the equivalence ratio, the flame temperature increases and more NO_x is produced. If NO_x is reduced by increasing the equivalence ratio, the flame temperature lowers and soot production increases. Figure 1 also shows two different low-temperature combustion paths. A typical homogeneous charge compression ignition path, where the fuel/oxidizer is well mixed before combustion

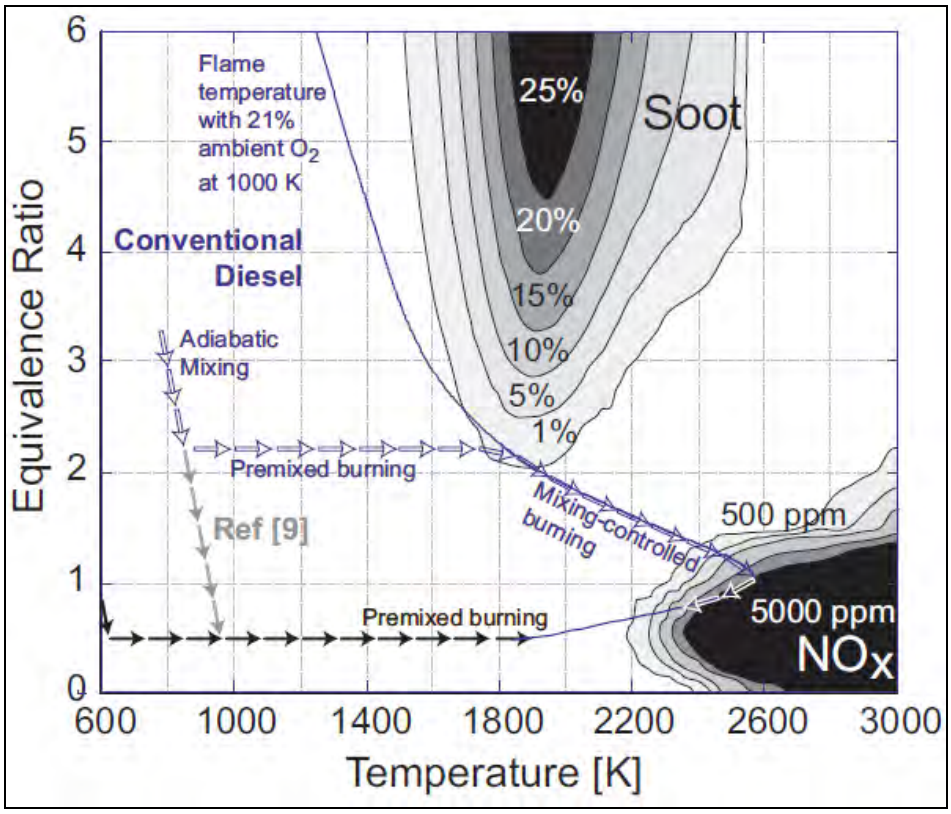

Figure 1. Soot and NO_x regions within an equivalence ratio/temperature plane showing conventional diesel and different low-temperature combustion processes (Kook et al., 2005).

occurs, is represented by the black arrows. The other combustion pathway, represented by gray arrows, occurs when lean equivalence ratios are attained by the continuation of high rates of mixing after premixed burning has started. A comparison of the low-temperature combustion processes to the conventional diesel process on the equivalence ratio/temperature plane reveals that soot and NO_x production are reduced when low-temperature combustion occurs.

C_2H_4 was chosen as a fuel for this study because of its abundance found during the combustion process of conventional fuels. During the oxidation of aliphatic hydrocarbons, such as n-dodecane ($C_{12}H_{26}$), n-decane ($C_{10}H_{22}$), and C_7H_{16}, C_2H_4 is an intermediate species (Ciajolo and D'Anna, 1998; Kurman et al., 2011; Olchanski et al., 2006). The oxidation process of hydrocarbons includes many intermediate species. As the molecular weight of a hydrocarbon increases, the number of intermediate species also increases. The increase in intermediate species makes studying the combustion chemistry of higher-molecular-weight hydrocarbons a challenging task. Therefore, understanding the combustion processes involved in the oxidation of C_2H_4 is a foundation to understanding the combustion of higher-molecular-weight hydrocarbons, which are used as practical fuels in power systems.

4. Experiment and Modeling

Flame studies were conducted with an opposed flow diffusion flame burner constructed out of 304 stainless steel. Opposed flow flame configurations are of interest to the combustion community because the configuration may be modeled as a one-dimensional (1-D) problem, and residence times can be readily adjusted (Turns, 2000). Additionally, this configuration allows for a comprehensive examination of different flame regimes. A detailed schematic of the burner and reaction zone is shown in figure 2. The burner is capable of operating at elevated and subatmospheric pressure conditions. However, for the experiments described in this study, the burner was operated at 1 atm. The burner includes an oxidizer and a fuel duct, each with a diameter of 16 mm. A 25.4-mm-diameter nitrogen (N_2) duct surrounds both the oxidizer and fuel ducts. The oxidizer and fuel ducts are arranged in a counter-flow configuration, with a duct separation of 6 mm. The compressed gases used for the flame studies consisted of C_2H_4 (purity of 99.9%) as fuel, air (zero grade) as oxidizer, and N_2 (purity of 99.999%). A multigas flow controller (MKS Instruments) was used to control the mass flow rates during the experiment.

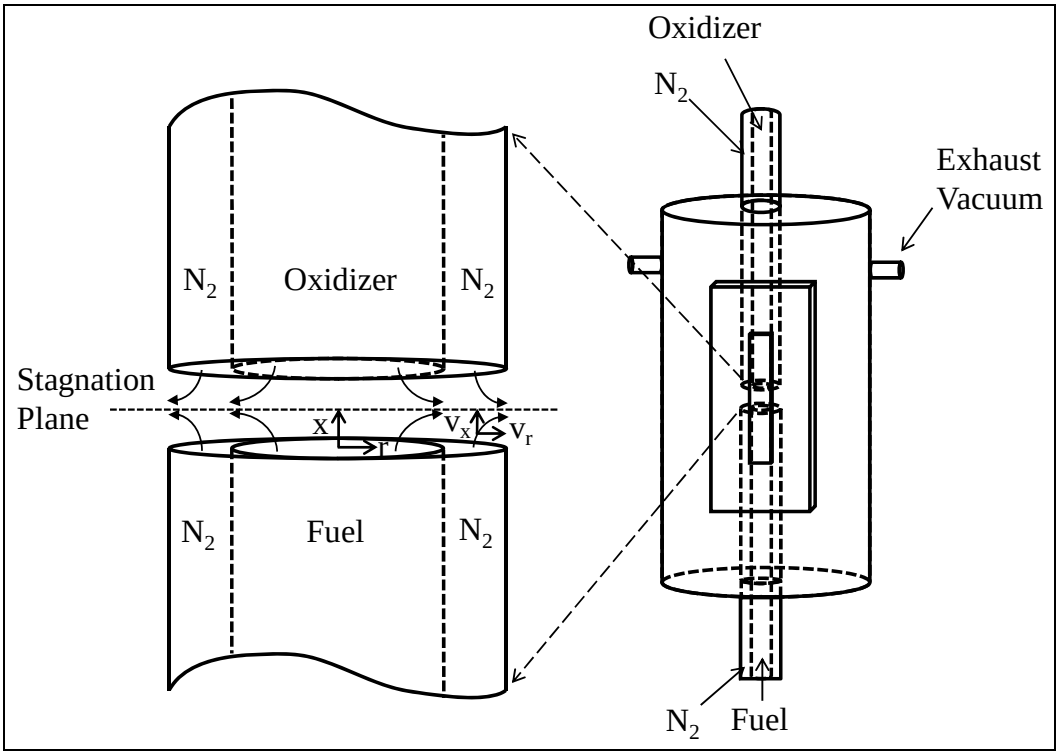

Figure 2. Schematic of the opposed flow diffusion flame burner with an enlarged view of the reaction zone. x and r are axial and radial directions, respectively. V_x and V_r are velocities in the axial and radial directions, respectively.

To acquire a stabilized flame, a pilot light was inserted between the oxidizer and fuel ducts prior to commencing fuel and oxidizer flow. Once inserted, the flow rates were adjusted to 2.5 standard liters per minute (SLPM) for C_2H_4, 2.0 SLPM for air, and 2.0 SLPM for N_2 shroud on the fuel duct. The calculated strain rate on the oxidizer side of the flame (i.e., a_2) was 123 s^{-1}, which is defined by equation 3:

$$a_2 = \frac{2|V_{ox}|}{L}\left(1+\frac{|V_f|\sqrt{\rho_f}}{|V_{ox}|\sqrt{\rho_{ox}}}\right), \tag{3}$$

where V_{ox}, L, V_f, ρ_f, and ρ_{ox} are the oxidizer velocity, duct separation, fuel velocity, fuel density, and oxidizer density, respectively (Seshadri and Williams, 1978). Once gas flow started, the burner would light and the opposed flow diffusion flame would be visible. To ensure that the flame was stabilized, measurements were not taken for ~5 min after ignition. Water was allowed to flow through the upper assembly of the burner, near the exhaust, for cooling. A vacuum pump extracted the exhaust from the burner chamber. Figure 3 shows a representation of the opposed flow diffusion flame. A visible blue region is present when the fuel diffuses into the oxidizer stream and stoichiometric combustion occurs. A visible red/orange region is present where fuel-rich combustion/fuel pyrolysis occurs. The blue region is attributed to light emission from CH and diatomic carbon (C_2) radicals, whereas the red/orange region is associated with soot incandescence.

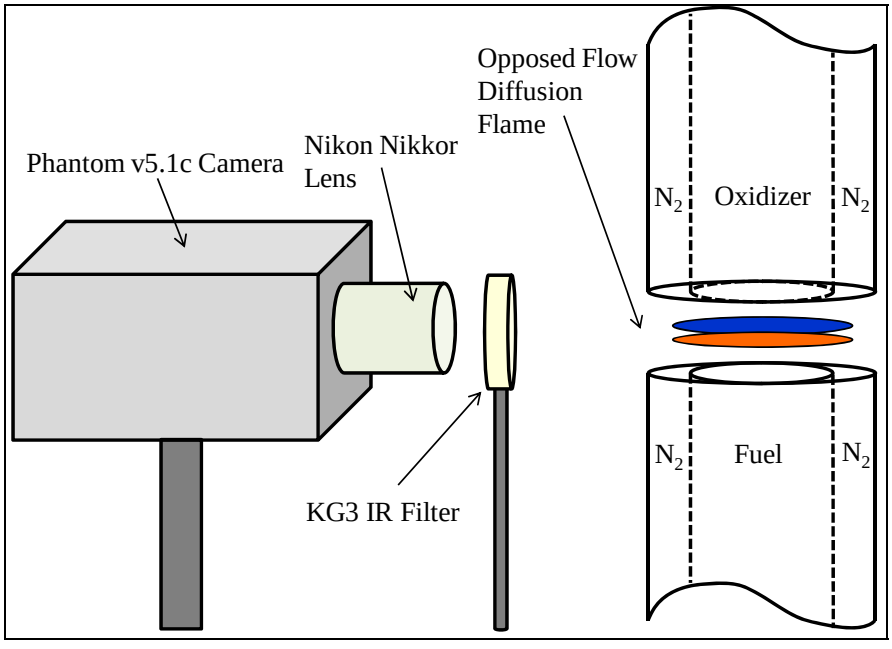

Figure 3. Camera setup for acquiring images of opposed flow diffusion flames.

Flame imaging was conducted with a Phantom v5.1c high-speed color camera manufactured by Vision Research Inc. Figure 3 also shows the camera setup used to image an opposed flow diffusion flame. A photograph of the experimental setup is shown in figure 4. The camera uses an 8-bit complementary metal oxide semiconductor (CMOS) imaging sensor with 1024 × 1024 pixels. At full resolution, the camera is capable of capturing 1200 frames per second (fps). However, during the flame studies presented here, the sample rate was 10 fps to compensate for low light levels from the flame. The camera is coupled to a Nikon AF Nikkor 24-85 mm f/2.8-4D IF lens, which has a macro mode feature. To ensure near-infrared (IR) radiation was blocked from reaching the CMOS image sensor, a Schott KG3 IR cutoff filter was placed between the lens and flame.

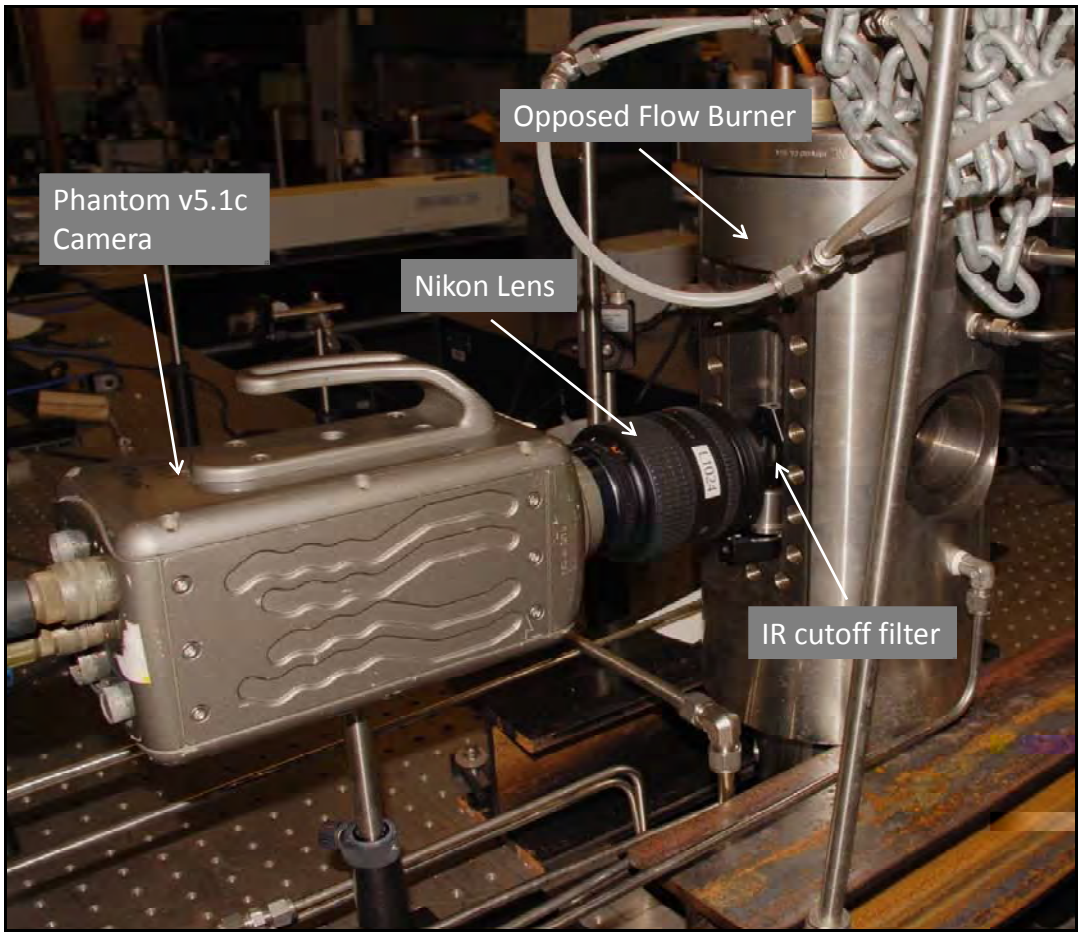

Figure 4. Photograph of the camera setup showing various components.

Pyrometry temperature measurements were accomplished using the Phantom v5.1c color camera. Using the light collected through a color filter array, a ratio of the green to red channels can be used to calculate the temperature of a flame. A gray body assumption, in which the variance in emissivity with wavelength is assumed to be constant, is also used in calculating the temperature. Additionally, errors in temperature measurements occur when discrete emission, such as C_2 or CH emission, is present in either spectral region used for the pyrometer measurement.

Interpretation of the pyrometry temperature measurements depends on the optical thickness of the flame. The camera images light from the surface of an optically thick flame. In such a flame, light from the interior of the flame is absorbed before it reaches the surface, and the interior flame temperature is not measured. In optically thin flames, light from the interior reaches the surface of the flame and is imaged by the camera. The measured temperature of an optically thin flame is a spatial average across the optical path.

Planck's law states that the spectral radiance, I, of a blackbody is dependent on the emissivity, ε, wavelength, λ, and temperature, T, where h is the Planck constant, c is the speed of light, and k is the Boltzmann constant, as shown in equation 4:

$$I(\lambda,T) = \varepsilon(\lambda,T)\frac{2\pi hc^2}{\lambda^5(e^{hc/\lambda kT}-1)} \ . \tag{4}$$

An analytical expression for the raw digital number from each sensor pixel is shown in equation 5,

$$D_{x,y} = \psi_i \Delta A_d \Delta\omega_d \Delta t \int \tau(\lambda) S(\lambda) \chi_i(\lambda) d\lambda \ , \tag{5}$$

where $D_{x,y}$ is the digital number from pixel (x, y), ψ_i is the gain of the camera electronics, ΔA_d is the area of a pixel, $\Delta\omega_d$ is the solid angle subtended by the pixel, Δt is the exposure time, $\tau(\lambda)$ is the transmission through the lens, $S(\lambda)$ is the input spectral radiation, $\chi_i(\lambda)$ is the color filter response for each channel, and the subscript i indicates the color filter (red, green, blue) of the pixel. A full color image is produced by using the raw image data and a simple mean filter (Densmore et al., 2011). To acquire a ratio of two color channels, equations 4 and 5 can be combined as shown in equation 6:

$$\frac{Green}{Red} = \frac{\psi_g \int I(\lambda,T)\chi_g(\lambda)d\lambda}{\psi_r \int I(\lambda,T)\chi_r(\lambda)d\lambda} \ . \tag{6}$$

Once the gain of the electronics (i.e., calibration factor) is calculated, a calibration curve can be established and unknown temperatures can be determined. Additional details of the two-color-ratio method used in this study have been described elsewhere (Densmore et al., 2011).

Thermocouple temperature measurements were conducted with an uncoated 0.051-mm-diameter Pt-Pt/10% Rh thermocouple. Each leg of the thermocouple was inserted through an alumina (Al_2O_3) tube to add support, and the legs were wired to a miniature ceramic connector. Once constructed, the thermocouple assembly was attached to a 3-axis (0.001-mm-resolution adjustment) translation stage for movement within the flame. A photograph of the thermocouple setup is shown in figure 5.

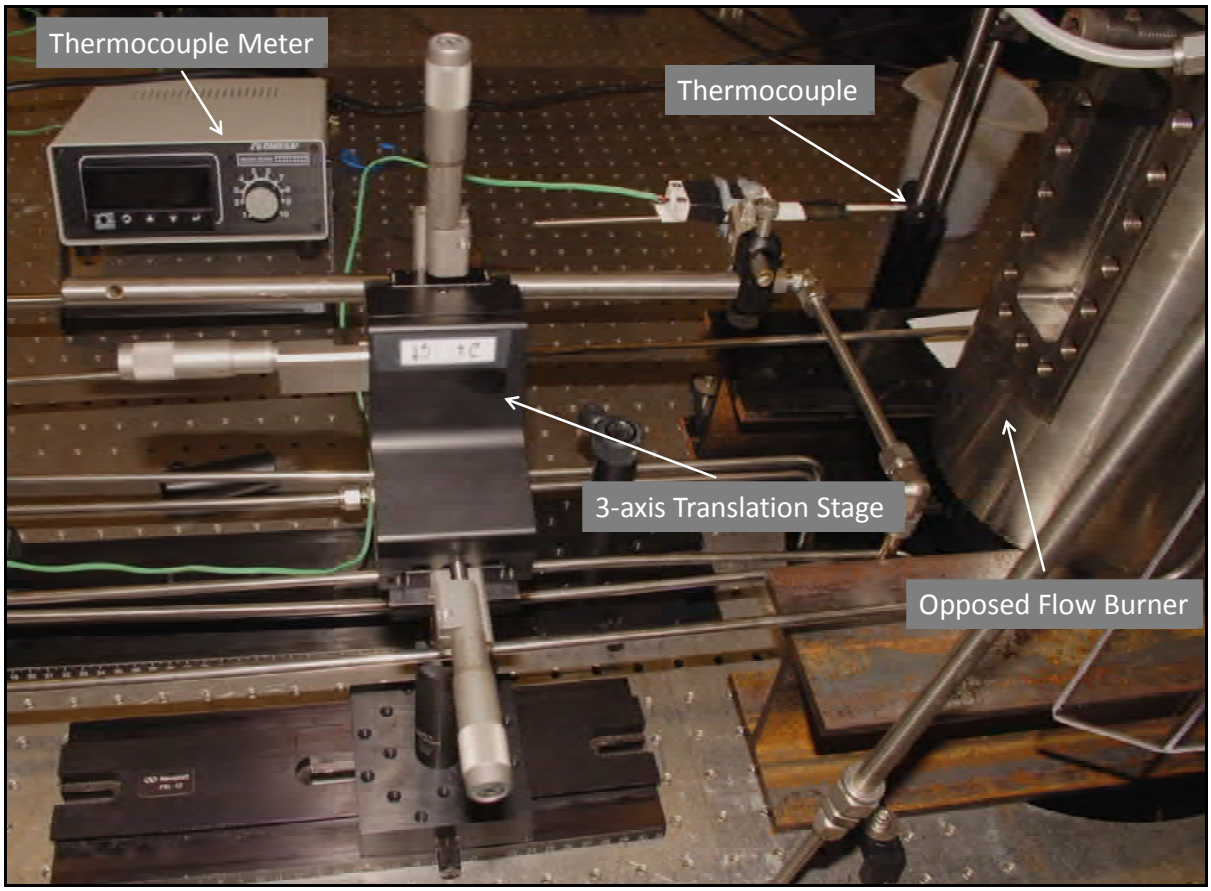

Figure 5. Photograph of the thermocouple setup showing various components.

Initially, the procedure to record the flame temperature was to insert and move the thermocouple from the lower fuel duct through the flame to the upper air duct. However, soot would accumulate on the thermocouple junction and cause inaccurate temperature readings. To prevent soot buildup on the junction, a new method was used. The new method consisted of inserting the thermocouple into the centerline of the flame, recording the temperature, and immediately removing the thermocouple. Dwell time of the thermocouple in the flame region was ~2 s. Once removed from the flame, the thermocouple was inspected for soot deposits. If soot deposits were found, they were removed by burning them off with an external flame source. To acquire a centerline temperature map of the flame, the vertical stage height was adjusted, and the insertion procedure was repeated. For the results presented in this study, the temperature measurements in the sooting region of the flame are an average of four experiments with a maximum error in the measurements of 20 K, based on ±1 standard deviation. The nonsooting region data are from one experiment.

Chemical kinetic modeling was performed using the Appel, Bockhorn, and Frenklach (ABF) mechanism, which contains 101 species, 544 reactions, and associated thermodynamic and transport files (Appel et al., 2000). The ABF mechanism was developed for soot formation and does not contain NO_x chemistry. The ABF mechanism has been validated with ethane (C_2H_6),

C_2H_4, and C_2H_2 as fuels, and it predicts major, minor, and aromatic species up to pyrene ($C_{16}H_{10}$). Cantera, which is an open source, multiplatform software code used to study combustion behavior, was used in conjunction with the programming language Python to execute the ABF mechanism (Goodwin, 2011). The modeling effort was conducted with a 1-D counter-flow flame object to simulate the opposed flow burner configuration. Initial conditions for the model simulation are shown in table 1. Initial grid spacing between the inlets for the simulation was set to 0.0, 0.06, 0.12, 0.18, 0.24, 0.30, 0.36, 0.48, 0.6 cm. After a Newton iteration was successfully converged, grid refinement was enabled and new grid points were inserted to continue with the simulation. The relative and absolute steady-state tolerances for convergence were set to 1.0×10^{-5} and 1.0×10^{-9}, respectively, and the relative and absolute tolerances for time stepping were set to 1.0×10^{-4} and 1.0×10^{-9}, respectively. A 2.67-GHz Intel Core* i5 processor with a 32-bit Windows operating system showed that the computational time for convergence to occur was 90 s with a total final grid count of 162.

Table 1. Initial conditions for the Cantera simulation. The mass flux of the fuel and oxidizer corresponds to the flow rates of the experiment and dimensions of the burner.

Parameter	Setting
Pressure	1 atm
Fuel and oxidizer temperature	300 K
Mass flux fuel (C_2H_4)	0.24 kg/m^2/s
Mass flux oxidizer (air)	0.20 kg/m^2/s
Duct separation	0.6 cm

5. Results and Discussion

A photograph of the C_2H_4/air-opposed flow diffusion flame at 1-atm pressure is shown in figure 6a. A notable characteristic of the opposed flow configuration is that two separate flame regions can be observed as the blue and red colors in the flame. The blue region is associated with emission from CH and C_2, whereas the red region is associated with soot incandescence. Figure 6b shows the surface temperature acquired from the pyrometry temperature measurement technique. The surface temperature of the C_2H_4/air in the sooting red/orange region of the flame is ~2000 K. As previously mentioned, the pyrometry technique is valid only when the gray body assumption holds and when discrete emission is minimal. Therefore, the temperature measurements in the blue region with emission from CH and C_2 are incorrect.

*Intel Core is a registered trademark of Intel Corporation.

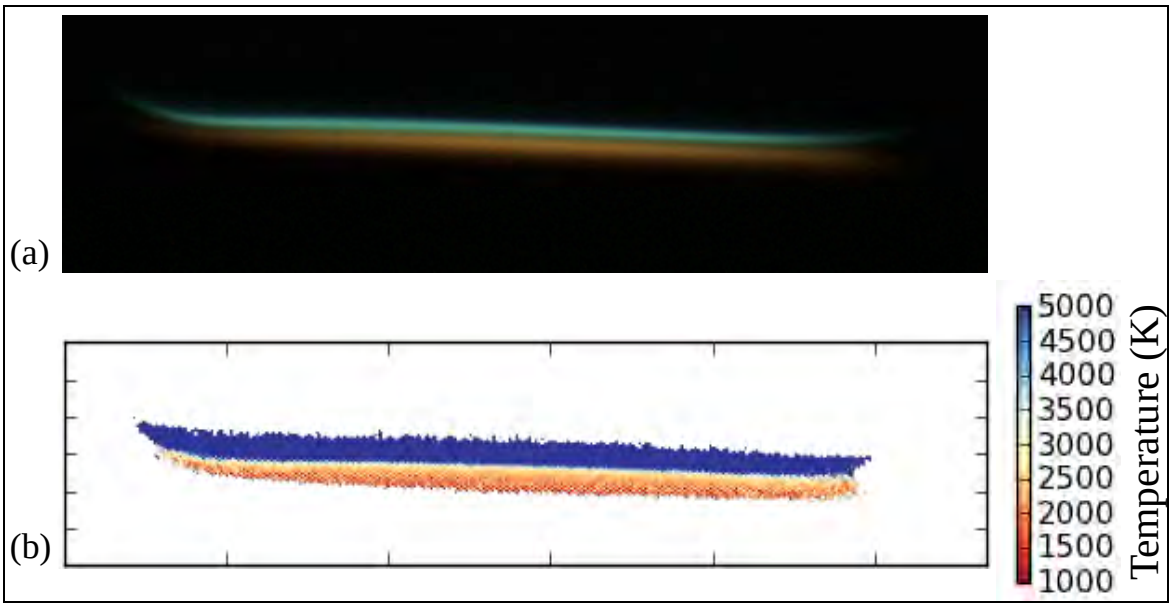

Figure 6. (a) Picture of the C_2H_4/air-opposed flow diffusion flame. (b) Reconstructed image showing the surface temperature of the C_2H_4 flame. The incorrect temperature in the blue region is caused by discrete emission.

Figure 7 shows a comparison of the pyrometry and thermocouple measurements, and a simulation calculated using Cantera. The pyrometry temperature measurements are a surface edge temperature ranging from the lower fuel duct to the upper air duct. In a plane located ~2 mm above the fuel duct (normal to the centerline between ducts), soot incandescence is present with a measured temperature of ~2000 K. The soot surface temperature increases as the fuel diffuses into the air stream. However, as mentioned previously, the pyrometry temperature measurements are erroneous in regions of the flame where discrete emission is present. The invalid temperatures caused by discrete emission between ~2.4 and 3.3 mm from the fuel duct are shown in figure 7. Additionally, discrepancies between the thermocouple measurements and pyrometer measurements of the surface temperature can also be caused by discrete emission. Further work needs to be performed to assure discrete emission is not affecting the pyrometry temperature measurements near the surface of the sooting region. The error in the pyrometer temperature measurements is approximately ±100 K. This error is from the uncertainty in the spectral transmission through the optical components and measured signal to noise.

Thermocouple temperature measurements are shown in figure 7. The temperature measurements between 2.20 and 3.20 mm above the fuel duct (i.e., sooting region) are an average of four experiments. Based on ±1 standard deviation of the measured temperatures, the maximum error in the measurements is 20 K. The thermocouple temperature measurements above 3.20 mm are from one experiment. The first measurement was 2.20 mm above the fuel duct with a temperature of 802 K. The temperature increased throughout the sooting region, moving toward the oxidizer duct, to a maximum temperature of 1898 K at 3.70 mm above the fuel duct. In this region, the flame appeared blue. Beyond 3.70 mm, toward the air duct, the flame temperature

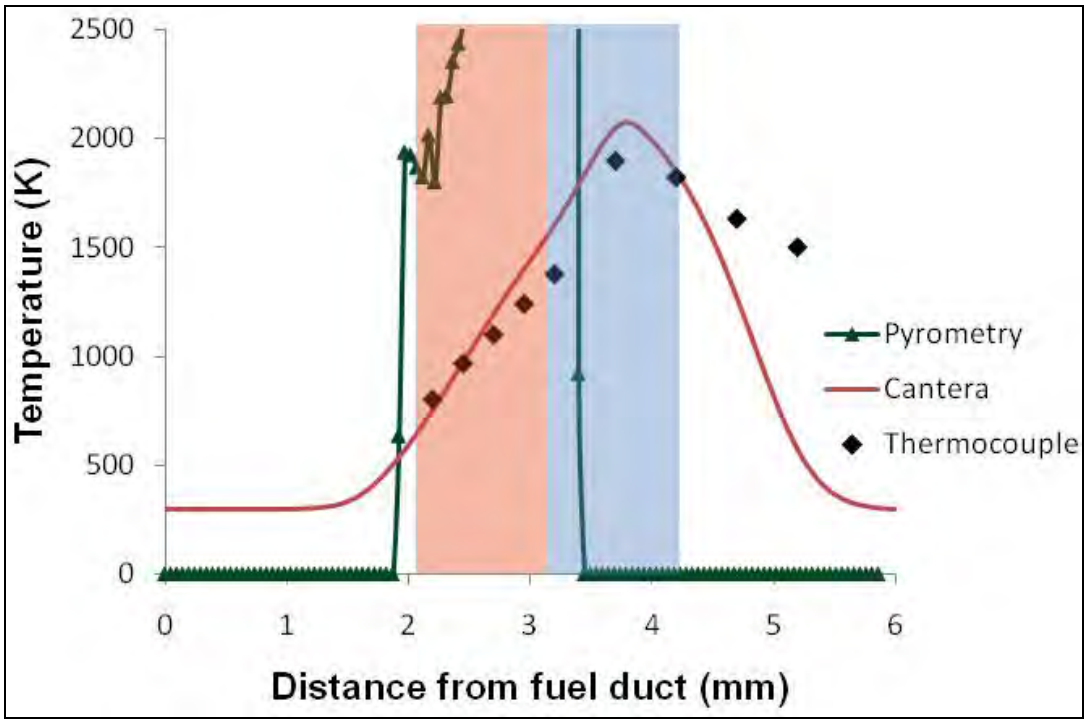

Figure 7. Comparison of the Cantera simulation with the results of the pyrometry and thermocouple temperature measurements. The blue and red regions represent locations of visible light produced from the flame.

decreased. Temperature measurements were taken up to 5.20 mm from the fuel duct. The arrangement of the thermocouple assembly prevented further measurements nearer to the air duct. However, it was expected that the temperature would decrease, as no flame was present in this region.

Similar experiments were performed by Olten and Senkan (1999) at atmospheric pressure with opposed-flow C_2H_4 diffusion flames. However, the calculated strain rate and duct separation for their study was 37.7 s^{-1} and 15 mm, respectively. Their thermocouple temperature measurements were recorded throughout the range of the fuel and oxidizer duct, and a maximum temperature of 1850 K was recorded. The thermocouple measurements by Olten and Senkan did not include corrections for radiation loss, similar to the results presented in this study. The radiation correction was left to the reader since additional uncertainties in the measured temperature can be introduced. A similar temperature profile was shown by the results of Olten and Senkan and the results presented in this study.

Figure 8 shows simulation results from executing the ABF mechanism with Cantera. The temperature increases at ~1.5 mm from the fuel duct. The temperature continues to increase throughout the red/orange sooting region of the flame until a maximum temperature of 2077 K at 3.79 mm is reached. The temperature then decreases toward the air duct. Concentration profiles of intermediate species produced during the combustion event are also shown in figure 8. The modeling simulation captures the two distinct regions, which were experimentally observed with

the opposed flow flame. Throughout the red/orange regime, soot incandescence is responsible for the color of the flame. The Cantera simulation shows the formation of soot precursors, such as C_2H_2 and C_6H_6. The local equivalence ratio is also shown in figure 8. The maximum production of soot precursors occurs at local equivalence ratios >1, which indicates that soot is formed in the fuel-rich region of the opposed flow flame. Additionally, the simulation shows the formation of CH and OH in the high-temperature regime where the blue color of the flame is observed. Simulations of a similar opposed flow diffusion flame system using the CHEMKIN software package conducted by McNesby et al. (2005) showed nearly identical results, as those predicted by Cantera in this study.

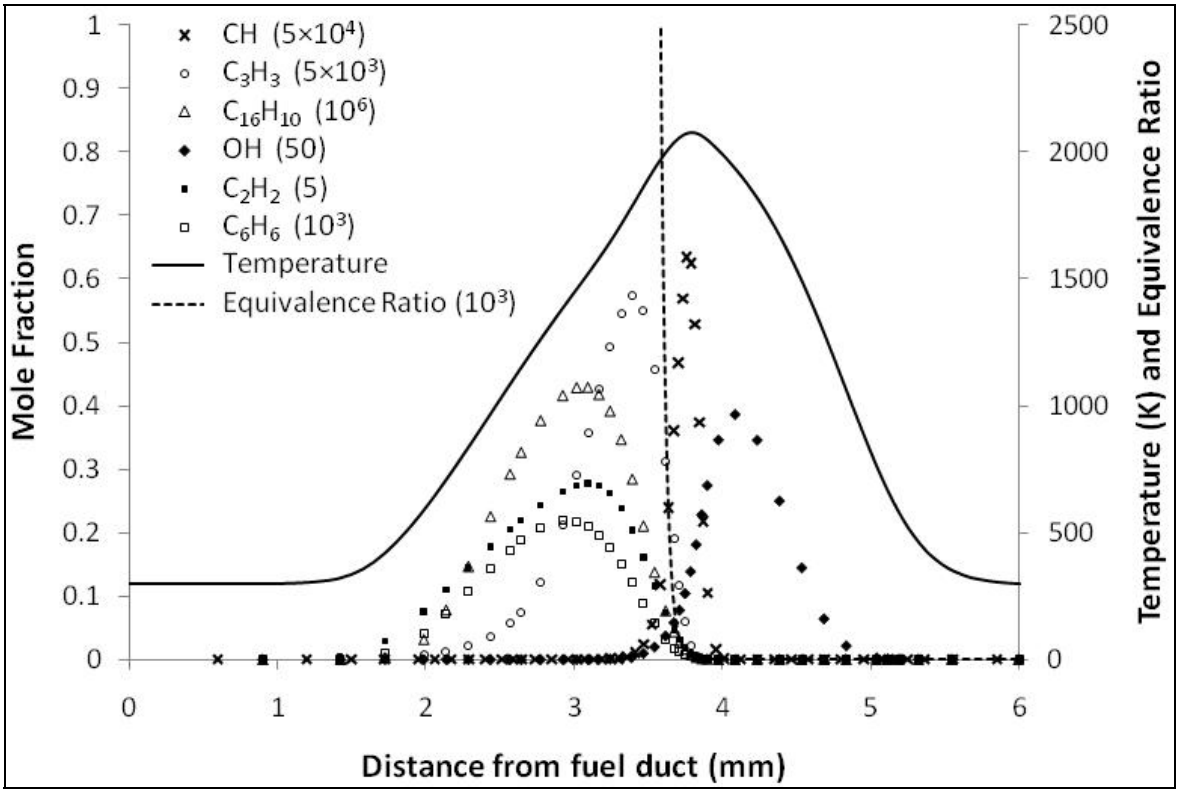

Figure 8. Simulation results from Cantera showing intermediate species produced during combustion, temperature profile, and local equivalence ratio. The multiplication factors are listed in parentheses.

Figure 9 shows a representation of figure 1, which is from Kook et al. (2005). In addition to the soot region, NO_x region, and typical diesel combustion pathway, figure 9 also shows the results of the Cantera calculation for local equivalence ratio with a C_2H_4/air flame at different pressures. The modeling results show that as pressure increases, the flame temperature also increases, thus moving the pathway toward the higher temperature NO_x region. However, the modeling effort does not include heat loss from soot radiation, which, if included, would cause the flame temperature to decrease as pressure increases. Each simulation at a different pressure yields a combustion pathway that lies in the sooting region. Therefore, using an opposed flow flame burner is an effective way to examine soot formation regions in a flame.

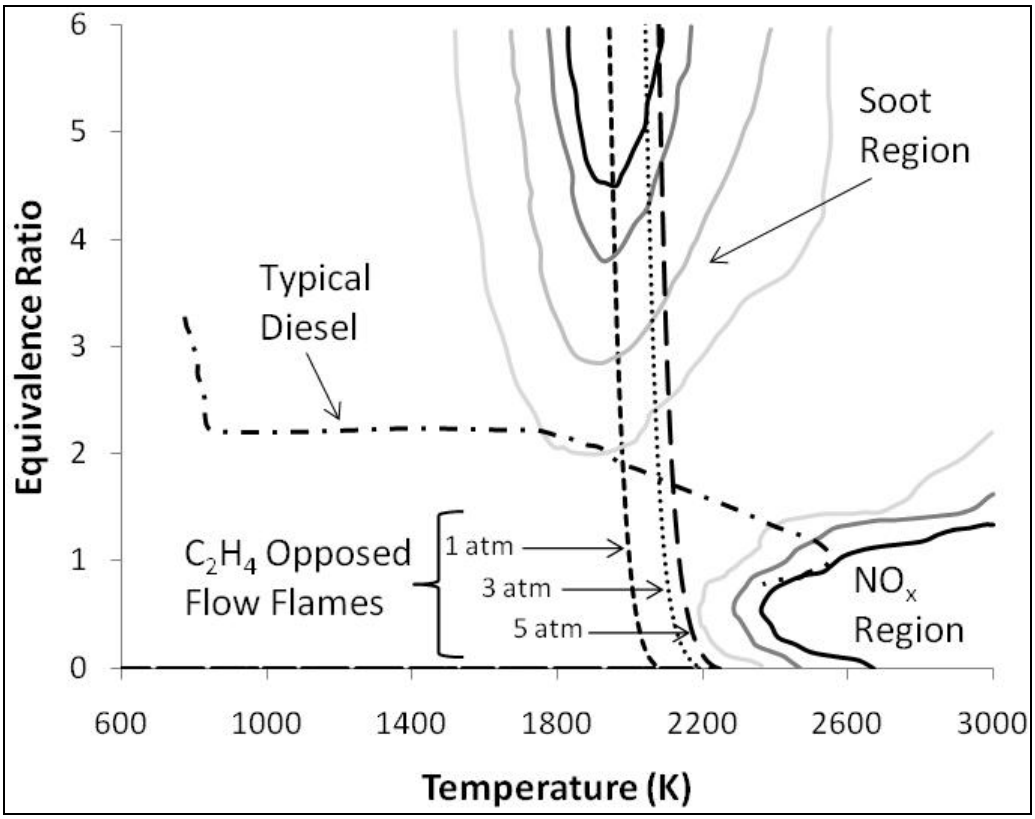

Figure 9. Representation of soot and NO_x regions within an equivalence ratio/temperature plane showing Cantera simulations for different pressures.

6. Conclusions

Temperature measurements of a C_2H_4/air-opposed flow diffusion flame were recorded experimentally by both optical pyrometry and thermocouple techniques. Optical pyrometry is a nonintrusive method for determining flame temperatures and does not interfere with the combustion chemistry of the flame. The pyrometry technique allows for an accurate temperature measurement only in regions of the flame where soot incandescence is occurring. In other regions of the flame where discrete emission is observed, the pyrometry temperature measurements are invalid. The Cantera modeling results predicted the temperature profile of the opposed flow flame, and the results from the thermocouple measurements showed a general trend. Additionally, the intermediate species responsible for soot production and the distinct color regions of the flame were also predicted by Cantera.

To our knowledge, this is the first detailed study comparing temperature measurements acquired from a single high-speed color camera pyrometer to thermocouple measurements and Cantera simulations for opposed flow diffusion flames. However, digital single lens reflex still-frame cameras have been reported as coflow flame pyrometers (Kuhn et al., 2011). The development

of a high-speed color camera as a pyrometer may allow scientists to investigate flame temperatures during dynamic events, such as flame extinguishment, turbulence, and rapid changes in fuel/oxidizer composition. Overall, the research results presented in this study will help to refine and validate chemical kinetic models for soot, which ultimately can lead to cleaner burning and more fuel-efficient power systems.

7. References

Appel, J.; Bockhorn, H.; Frenklach, M. Kinetic Modeling of Soot Formation With Detailed Chemistry and Physics. Laminar Premixed Flames of C_2 Hydrocarbons. *Combustion and Flame* **2000**, *121* (1–2), 122–136.

Ciajolo, A.; D'Anna, A. Controlling Steps in the Low-Temperature Oxidation of n-Heptane and iso-Octane. *Combustion and Flame* **1998**, *112* (4), 617–622.

Densmore, J. M.; Biss, M. M.; McNesby, K. L.; Homan, B. E. High-Speed Digital Color Imaging Pyrometry. *Applied Optics* **2011**, *50* (17), 2659–2665.

Edwards, T.; Maurice, L. Surrogate Mixtures to Represent Complex Aviation and Rocket Fuels. *Journal of Propulsion and Power* **2001**, *17* (2), 461–466.

Frenklach, M. Reaction Mechanism of Soot Formation in Flames. *Physical Chemistry Chemical Physics* **2002**, *4* (11), 2028–2037.

Glass, D.; Gray, C.; Jolley, D.; Gibbons, C.; Sim, M.; Fritschi, L.; Adams, G.; Bisby, J.; Manuell, R. Leukemia Risk Associated With Low-Level Benzene Exposure. *Epidemiology* **2003**, *14* (5), 569–577.

Goodwin, D.; Cantera, G. Suite of Object-Oriented Software Tools for Problems Involving Chemical Kinetics, Thermodynamics, and/or Transport Processes. http://code.google.com/p/cantera (accessed 8 August 2011).

International Agency for Research on Cancer (IARC). Overall Evaluations of Carcinogenicity: An Updating of IARC Monographs Vol. 1 to 42. *IARC Monographs on the Evaluation of Carcinogenic Risks to Humans* **1987**, Suppl. 7, 120–122.

Kitamura, T.; Ito, T.; Senda, J.; Fujimoto, H. Mechanism of Smokeless Diesel Combustion With Oxygenated Fuels Based on the Dependence of the Equivalence Ratio and Temperature on Soot Particle Formation. *International Journal of Engine Research* **2002**, *3* (4), 223–248.

Kook, S.; Bae, C.; Miles, P. C.; Choi, D.; Pickett, L. M. The Influence of Charge Dilution and Injection Timing on Low-Temperature Diesel Combustion and Emissions. Society of Automotive Engineers (SAE) International, 2005-01-3837, 2005.

Kuhn, P. B.; Ma, B.; Connelly, B. C.; Smooke, M. D.; Long, M. B. Soot and Thin-Filament Pyrometry Using a Color Digital Camera. *Proceedings of the Combustion Institute* **2011**, *33* (1), 743–750.

Kurman, M. S.; Natelson, R. H.; Cernansky, N. P.; Miller, D. L. Speciation of the Reaction Intermediates From n-Dodecane Oxidation in the Low Temperature Regime. *Proceedings of the Combustion Institute* **2011**, *33* (1), 159–166.

McNesby, K. L.; Miziolek, A. W.; Nguyen, T.; Delucia, F. C.; Skaggs, R. R.; Litzinger, T. A. Experimental and Computational Studies of Oxidizer and Fuel Side Addition of Ethanol to Opposed Flow Air/Ethylene Flames. *Combustion and Flame* **2005**, *142* (4), 413–427.

MIL-DTL-83133G. *Detail Specification: Turbine Fuel, Aviation, Kerosene Type, JP-8 (NATO F-34), NATO F-35, and JP-8+100 (NATO F-37)* **30 April 2010**.

Miller, J.; Melius, C. Kinetic Thermodynamic Issues in the Formation of Aromatic Compounds in Flames of Aliphatic Fuels. *Combustion and Flame* **1992**, *91* (1), 21–39.

Olchanski, E.; Burcat, A. Decane Oxidation in a Shock Tube. *International Journal of Chemical Kinetics* **2006**, *38* (12), 703–713.

Olten, N.; Senkan, S. Formation of Polycyclic Aromatic Hydrocarbons in an Atmospheric Pressure Ethylene Diffusion Flame. *Combustion and Flame* **1999**, *118* (3), 500–507.

Rinsky, R. Benzene and Leukemia: An Epidemiologic Risk Assessment. *Environmental Health Perspectives* **1989**, *82*, 189–191.

Seshadri, K.; Williams, F. A. Laminar Flow Between Parallel Plates With Injection of a Reactant at High Reynolds Number. *International Journal of Heat and Mass Transfer* **1978**, *21* (2), 251–253.

Turns, S. R. *An Introduction to Combustion Concepts and Applications,* 2nd ed.; McGraw-Hill: New York, 2000.

List of Symbols, Abbreviations, and Acronyms

1-D	one dimensional
a_2	strain rate on the oxidizer side of flame
ΔA_d	area of pixel
ABF	Appel, Bockhorn, and Frenklach
atm	atmosphere
c	speed of light
C_2	diatomic carbon
C_2H_2	acetylene
C_2H_4	ethylene
C_2H_6	ethane
C_3H_3	propargyl
C_6H_6	benzene
C_7H_{16}	n-heptane
$C_{10}H_{22}$	n-decane
$C_{12}H_{26}$	n-dodecane
$C_{16}H_{10}$	pyrene
CH	methylidyne
cm	centimeter
CMOS	complementary metal oxide semiconductor
D	measured signal from camera
ε	emissivity

fps	frames per second
GHz	gigahertz
h	Planck constant
H_2	hydrogen
i(subscript)	color filter of a pixel
I	spectral radiance
IR	infrared
k	Boltzmann constant
K	Kelvin
kg	kilogram
λ	wavelength
L	duct separation
m	meter
mm	millimeter
MPa	megapascal
ms	millisecond
N_2	nitrogen
OH	hydroxyl
PAH	polycyclic aromatic hydrocarbon
ρ_f	fuel density
ρ_{ox}	oxidizer density
Pt	platinum
Rh	rhodium

ψ_i	gain of camera electronics
s	second
$S(\lambda)$	input spectral radiation
SLPM	standard liters per minute
Δt	exposure time
T	temperature
$\tau(\lambda)$	transmission through lens
V_f	fuel velocity
V_{ox}	oxidizer velocity
$\Delta\omega_d$	solid angle subtended by pixel
$\chi_i(\lambda)$	color filter response of each channel

NO. OF COPIES	ORGANIZATION
1 (PDF only)	DEFENSE TECHNICAL INFORMATION CTR DTIC OCA 8725 JOHN J KINGMAN RD STE 0944 FORT BELVOIR VA 22060-6218
1	DIRECTOR US ARMY RESEARCH LAB IMNE ALC HRR 2800 POWDER MILL RD ADELPHI MD 20783-1197
1	DIRECTOR US ARMY RESEARCH LAB RDRL CIO LL 2800 POWDER MILL RD ADELPHI MD 20783-1197
1	DIRECTOR US ARMY RESEARCH LAB RDRL CIO MT 2800 POWDER MILL RD ADELPHI MD 20783-1197
1	DIRECTOR US ARMY RESEARCH LAB RDRL D 2800 POWDER MILL RD ADELPHI MD 20783-1197

NO. OF
COPIES ORGANIZATION

1 LAWRENCE LIVERMORE NATIONAL
LABORATORY
J DENSMORE
7000 EAST AVE L-227
LIVERMORE CA 94550

ABERDEEN PROVING GROUND

9 DIR USARL
RDRL VT
M VALCO
RDRL VTP
W ACOSTA
M KURMAN
C KWEON
RDRL WMP G
B HOMAN
RDRL WML B
R PESCE-RODRIGUEZ
R SAUSA
RDRL WML C
K MCNESBY
M BISS

INTENTIONALLY LEFT BLANK.